Available online at www.sciencedirect.com
SCIENCE DIRECT
Journal of Solid State Chemistry 179 (2006) 2339–2348
JOURNAL OF SOLID STATE CHEMISTRY
www.elsevier.com/locate/jssc

Synthesis and characterisation of hexagonal molybdenum nitrides

Alexey Yu. Ganin[a,1], Lorenz Kienle[a], Grigori V. Vajenine[a,b,*]

[a]*Max-Planck-Institut für Festkörperforschung, Heisenbergstraße 1, 70569 Stuttgart, Germany*
[b]*Institut für Anorganische Chemie, Universität Stuttgart, Pfaffenwaldring 55, 70569 Stuttgart, Germany*

Received 10 April 2006; received in revised form 23 May 2006; accepted 25 May 2006
Available online 2 June 2006

Dedicated to Hans-Georg von Schnering on the occasion of his 75th birthday

Abstract

Four hexagonal molybdenum nitrides—three modifications of δ-MoN and Mo_5N_6—were prepared by the plasma-enhanced chemical vapour deposition (PECVD) method and ammonolysis of $MoCl_5$ and MoS_2. The nitrides were structurally characterised by X-ray diffraction, high-resolution transmission electron microscopy, and selected area electron diffraction. δ_1-MoN is best described by the WC-type structure with stacking faults due to nitrogen atom disorder. Ordering of nitrogen atoms results in δ_2-MoN with the NiAs-type structure. Formation of trigonal molybdenum clusters in δ_3-MoN is responsible for the doubling of the unit cell in a and b directions compared to δ_2-MoN. Mo_5N_6 can be viewed as an intergrowth structure of the WC- and NiAs-type building blocks, accompanied by vacancies on Mo sites. Influence of reaction conditions on the formation of the four nitrides is discussed; their magnetic properties are presented.

Keywords: Molybdenum nitrides; Plasma-enhanced chemical vapour deposition (PECVD); Ammonolysis; Powder X-ray diffraction; Crystal structure investigations; High-resolution transmission electron microscopy (HRTEM); Selected area electron diffraction (SAED)

1. Introduction

There are at least four hexagonal molybdenum nitrides known from the literature: three modifications of δ-MoN and Mo_5N_6.

δ_1-MoN can be synthesised by a reaction of $MoCl_5$ with ammonia [1] or by plasma-enhanced chemical vapour deposition (PECVD) from the nitrogen plasma using $MoCl_5$ as a precursor [2] in the temperature range of 500–650 °C. This nitride was described by Lengauer as having a WC-type crystal structure (space group $P\bar{6}m2$, $a = 285.1$ pm, $c = 278.2$ pm, $Z = 1$) though it appears to have a more complicated crystal structure due to the disorder of the nitrogen atom layers along the c-axis [3].

δ_2-MoN can be prepared from nitrogen and $MoCl_5$ by PECVD at the temperature of 730 °C [2]. According to selected area electron diffraction (SAED), it crystallises with the NiAs-type structure (space group $P6_3/mmc$, $a = 286$ pm, $c = 569$ pm, $Z = 2$) and forms separate domains grown together with the previously known and much investigated δ_3-MoN.

δ_3-MoN can be prepared by a reaction of Mo metal with ammonia at 700 °C and has been characterised by Hägg [4] with a hexagonal unit cell ($a = 290.1$ pm, $c = 283.0$ pm). However, some additional weak reflections in the diffraction pattern, first attributed by Hägg to impurities, indicated the formation of a superstructure. In fact, these weak reflections were interpreted by Schönberg assuming a $2 \times 2 \times 2$ supercell with the space group $P6_3/mmc$ ($a = 572.5$ pm, $c = 560.8$ pm; $Z = 8$) for this nitride [5]. In the proposed structure $\frac{3}{4}$ of all molybdenum atoms are shifted from their idealised positions to build triangular clusters and the rest occupy the special $2a$ position. In this structural model, the nitrogen atoms are statistically distributed in the centres of trigonal prisms formed by

*Corresponding author. Fax: +49 711 689 1091.
E-mail addresses: A.Ganine@fkf.mpg.de (A.Y. Ganin), L.Kienle@fkf.mpg.de (L. Kienle), G.Vajenine@fkf.mpg.de (G.V. Vajenine).
[1]Current address: Department of Chemistry, University of Liverpool, Liverpool L69 7ZD, UK.

0022-4596/$ - see front matter © 2006 Elsevier Inc. All rights reserved.
doi:10.1016/j.jssc.2006.05.025

metal atoms. Later, Bezinge et al. [6] prepared δ_3-MoN by high-pressure high-temperature annealing of δ_1-MoN and proposed the space group $P6_3mc$ ($a = 573.7$ pm, $c = 561.3$ pm, $Z = 8$) for the crystal structure. Here, the nitrogen atoms are situated in every second trigonal prismatic void built by metal atom layers (cf. Fig. 1). This structure introduces both clustering of the Mo atoms and ordering of N atoms so that the atomic arrangement can be described as a slightly deformed $2 \times 2 \times 1$ superstructure of the NiAs type. The space group $P6_3mc$ for the crystal structure of this nitride has been confirmed by neutron diffraction recently [7,8]. The fact that δ_3-MoN crystallises in the non-centrosymmetric space group $P6_3mc$ with triangular Mo clusters is rather unusual, but not unique. Its analogue is known in the literature: the low temperature modification of $NbS_{0.92}$ [9] features the same $2 \times 2 \times 1$ superstructure of the NiAs structure type. Similar as in the δ_3 phase of MoN, niobium atoms build triangular Nb_3 clusters in $NbS_{0.92}$. However, due to the larger size of sulphur atoms compared to nitrogen atoms, the intracluster distances in $NbS_{0.92}$ are almost the same (291.8 pm) as those found in Nb metal (292 pm). This is not the case in δ_3-MoN: here, the Mo–Mo distances within the clusters (267.1 pm [8]) are substantially shorter than that in Mo metal (280 pm). Owing to its unique physical properties, such as superconductivity at up to 12 K [7,8] and high hardness, δ_3-MoN has been intensively investigated by various authors. Detailed descriptions of properties and preparation techniques can be found in the following reviews (cf. Refs. [10,11]). Interestingly, the electronic structure of δ_3-MoN has been studied recently by DFT at LDA and GGA levels [12]; the optimised crystal structure was found to be consistent with those reported by Marchand et al. [7] and Bull et al. [8].

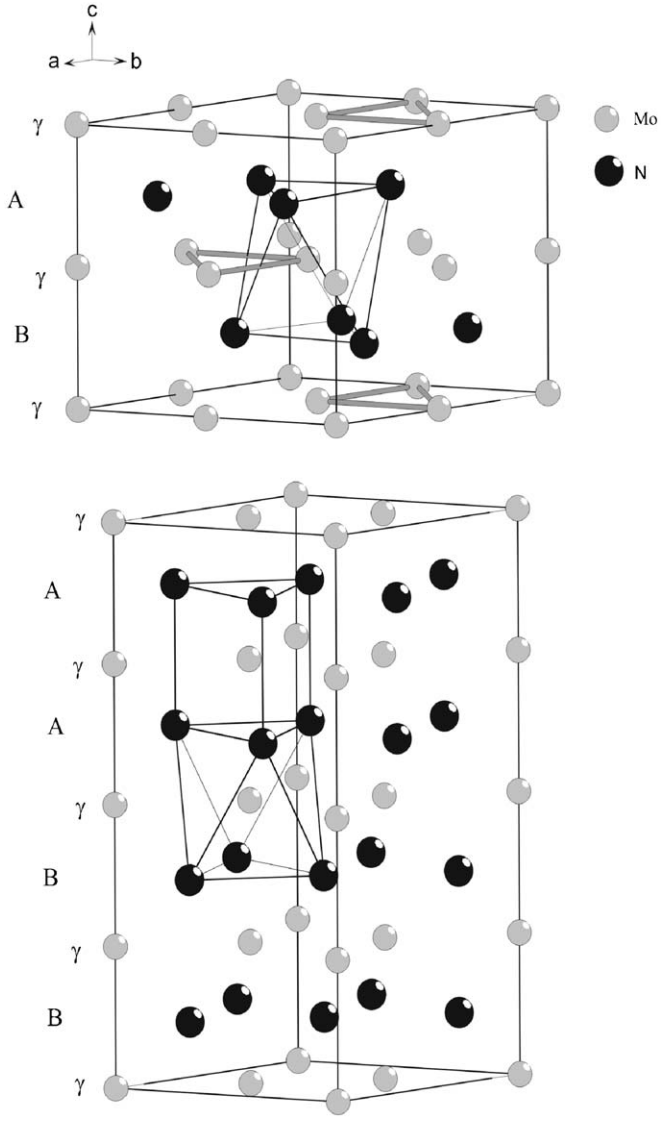

Fig. 1. Crystal structure of δ_3-MoN showing the octahedral coordination of Mo atoms and the Mo_3 clusters within the hexagonal unit cell (above); MoN_6 trigonal prismatic and octahedral units forming the crystal structure of Mo_5N_6 (below).

Another hexagonal molybdenum nitride was first reported in [13] and can be prepared by a reaction of thin Mo films with ammonia at 750 °C. Troitskaya and Pinsker reported this nitride with the composition $Mo_{0.82–0.85}N$ in the space group $P6_3/mmc$ ($a = 286$ pm, $c = 1120$ pm, $Z = 4$). Later, this nitride was characterised with a larger hexagonal unit cell: $a = 489.3$ pm ($\approx \sqrt{3}a_{\text{Troitskaya}}$), $c = 1106$ pm and the composition Mo_5N_6 [7]. Marchand et al. described the structure of Mo_5N_6 as one featuring an AABB … arrangement of N atoms. In this context, Mo_5N_6 can be viewed as an intergrowth product of the WC- and NiAs-type structures. The molybdenum atoms occupy all trigonal prismatic and $\frac{2}{3}$ of all octahedral voids formed by layers of N atoms, as in a filled MoS_2-type structure (cf. Fig. 1). However, the exact distribution of Mo atoms and vacancies in octahedral sites, as well as the choice of space group ($P6_3/m$ or $P6_322$) is still to be determined.

In our recent works [2,3], we have already discussed some aspects of crystal chemistry of hexagonal molybdenum nitrides. It was possible to obtain three different phases of hexagonal molybdenum nitride—δ_1-, δ_2-, and δ_3-MoN—using the PECVD method. However, from the last study some questions are still open. Is there a direct transformation of the δ_1 into the δ_3 phase under ambient pressure? Could δ_2-MoN be isolated phase pure and be prepared using conventional synthetic routes? Below we report results of our further investigations of the hexagonal molybdenum nitrides. In order to understand the complex structural chemistry of these nitrides, the laterally high-resolution methods high-resolution transmission electron microscopy (HRTEM) and SAED were employed in addition to X-ray diffraction.

2. Experimental section

2.1. Plasma-enhanced chemical vapour deposition

The PECVD setup used in our work consisted of four main parts: a gas delivery system, a precursor handling

system, a reactor, and a vacuum system. Nitrogen gas was first purified in the gas delivery system and then led into the precursor handling system with a flow rate of 60 cm^3/s. It was then mixed with the evaporated $MoCl_5$ (Strem Chemicals, 99.6%, additionally sublimated, purity controlled by X-ray diffraction [14]) precursor and introduced into the reactor chamber. Here, deposition occurred in a plasma region inside of a quartz glass tube between two parallel electrodes. This setup was placed in an evacuated glass vessel (work pressure 2 Torr). The upper electrode was connected to the radio frequency source (13.56 MHz) through a matchbox, while the bottom electrode was grounded and served as a substrate holder. The substrate temperature was controlled by a thermocouple, which was inserted into the bottom electrode. The deposition time was ca. 30–40 min. A more detailed description of the PECVD setup and experimental process can be found elsewhere [2,3,15].

Depositions were carried out on wafers of microcrystalline hexagonal boron nitride with a typical diameter of 20 mm and a thickness of 1 mm. The substrates were prepared for deposition by washing with ethanol in an ultrasonic bath and then rinsing them with distilled water and acetone.

Black in colour polycrystalline films with the thickness of ca. 2 μm were obtained. Where possible, all manipulations with the samples were carried out in an argon-filled glove box with the oxygen and water content of less than 1 ppm or using Schlenck technique. Chemical analysis of the films was not possible and thus their composition was analysed by EDXS directly on the substrate, and then by X-ray diffraction in reflection geometry. According to X-ray diffraction, phase pure films of δ_1-MoN can be deposited in the temperature range of 610–650 °C, while at higher temperatures (680–730 °C) films of δ_3-MoN were predominantly formed. Films **A** (prepared at 610 °C) and **B** (prepared at 730 °C) with the composition close to MoN according to EDXS could be separated from the substrate in a powder form. The sample amount on the 1–2 mg scale was used for further investigations by powder X-ray diffraction (PXRD) and HRTEM.

2.2. Ammonolysis of $MoCl_5$ and MoS_2

A series of bulk samples was prepared by ammonolysis of $MoCl_5$ or MoS_2 as described earlier [1,7]. In an argon-filled glove box, a Mo boat with 0.35–0.5 g MoS_2 (Riedel de-Haen, 99.55%) or $MoCl_5$, purified by a sublimation of the commercially available chloride (Strem Chemicals, 99.6%), was loaded into a quartz glass tube. The tube was then closed from both ends, put into a tube furnace and connected to the ammonia line. After adjusting the ammonia flow, the tube was heated to the final reaction temperature (Table 1). After cooling, the tube was opened in the glove box and black microcrystalline products were observed in the boat. As in the case of thin film samples, the products were treated as air sensitive compounds to prevent any contamination by oxygen. The reaction conditions and phase composition are summarised in Table 1.

2.3. Scanning electron microscopy (SEM) and energy-dispersive X-ray spectroscopy (EDXS)

Microstructure investigations were performed on a TESCAN 5120MM scanning electron microscope (SEM). Qualitative and half-quantitative analysis of samples was carried out by EDXS analysis with an Oxford Si-detector using electron beam energy of 10 keV and signal accumulation time of 60–120 s. Chlorine, sulphur, and oxygen contaminations were found to be below the detection limit of EDXS (2–3 at%).

2.4. Chemical analysis

For samples **C**, **D** and **F** chemical analysis for oxygen and nitrogen content was carried out using an Exhalograph EAO 220 (Balzers) analyser. The sample was loaded in a graphite capsule and then melted in vacuo by applying electrical pulse heating. The oxygen content was detected by IR absorption of carbon monoxide; the nitrogen content was detected using thermal conductivity measurements.

Table 1
Product composition and reaction conditions for selected samples

Phase Sample	δ_1-MoN **C**	Mo_5N_6 **D**	δ_3-MoN + Mo_5N_6 **E**	δ_3-MoN **F**
Precursor	$MoCl_5$	MoS_2	MoS_2	MoS_2
Reaction temperature (°C)	600	750	800	825
Reaction time (h)	3	40	21	20
Heating rate (°C/h)	600	600	600	600
Cooling rate	400	300	300	300
Ammonia flow (cm^3/min)	50	100	100	50
Oxygen content (wt%)[a]	0.4	0.7 (0.8)	<0.6[b,c]	0.5 (0.5)
Nitrogen content (wt%)[a]	12.9	14.9 (15.0)	14.2[b]	13.0 (13.2)

[a]Results reported earlier [7] are given in parentheses for comparison.
[b]From EDXS analysis.
[c]Detection limit.

2.5. PXRD studies

PXRD data was collected at room temperature on a STADI-P STOE diffractometer (Cu$K\alpha_1$ radiation, $\lambda = 154.056$ pm) operating in Debye–Sherrer geometry with a scanning step of 0.1° and signal accumulation of 25 s. The samples were grounded in a glove box with glass to reduce absorption and texture effects, and than sealed in thin-walled glass capillaries. Depending on the sample amount 0.1–0.3 mm capillaries were used.

The powder diffraction patterns recorded for **A** and **C** are shown in Fig. 2. For these samples, unit cell parameters were refined by simple square root algorithm using STOE WinXPOW software. The refinement results are summarised in Table 2.

The PXRD patterns of samples **B**, **D**, and **F** are illustrated in Figs. 3–5. These data were used for a Rietveld refinement using GSAS&EXPGUI software [16]. Pseudo-Voigt function [17] was employed to model reflection profiles. The background was fitted using a cosine Fourier series function and an absorption correction was introduced. Additionally, a texture effect was taken into account for **B** and **F**.

The crystal structure for δ_3-MoN (space group $P6_3mc$) first reported in [6] was chosen as the starting model for **B** and **F**. The unit cell constants and the atomic positional parameters were refined, while the isotropic temperature displacement factors had to be fixed at $U_{iso} = 50\,pm^2$ (cf. results in Tables 2–4). The refinement of the PXRD data carried out using the crystal structure reported earlier in [5] (centrosymmetric space group $P6_3/mmc$) gave even better results ($R_p = 6.14\%$; $R_{wp} = 5.02\%$). However, this model could not reproduce the 2 0 1 and 2 0 3 reflections properly, as has also been noted previously in [6]. Furthermore, the refinement within this structure required some additional peaks, which were missing in the diffraction pattern.

Although the systematic absences in the PXRD pattern of Mo_5N_6 (**D**) were consistent with the space groups $P6_322$

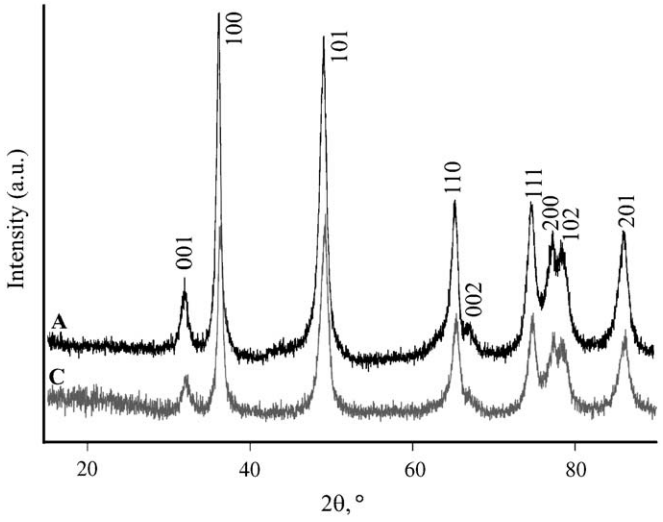

Fig. 2. Measured powder X-ray diffraction patterns of δ_1-MoN prepared from N_2 plasma and $MoCl_5$ by PECVD (**A**) and by ammonolysis of $MoCl_5$ (**C**).

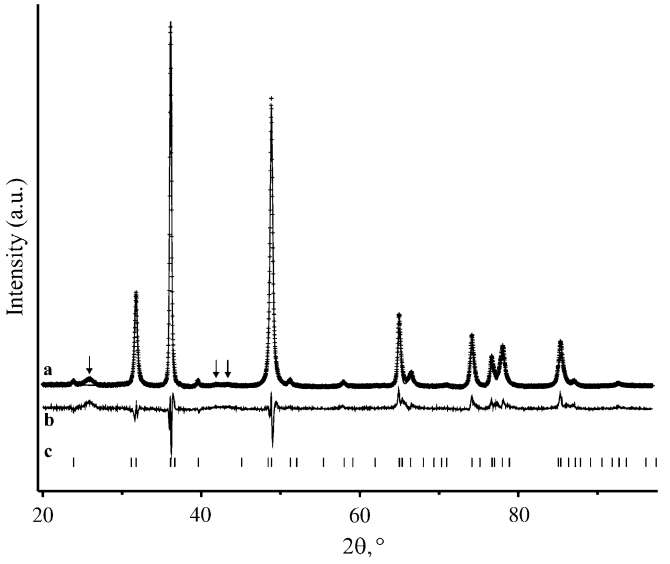

Fig. 3. Rietveld refinement results for the powder X-ray diffraction pattern of **B** prepared from N_2 plasma and $MoCl_5$ by PECVD: measured pattern (+) and the calculated curve for δ_3-MoN (solid line) (a). The difference between the two curves is plotted below (b) and the positions of reflections for the δ_3 phase are shown (c). Impurity reflections (BN from the substrate) are indicated with arrows.

Table 2
Details of the crystal structure refinement from powder X-ray diffraction data for δ_1-MoN, δ_3-MoN, and Mo_5N_6

Phase	δ_1-MoN		δ_3-MoN		Mo_5N_6
Sample	**A**	**C**	**B**	**F**	**D**
Space group	$P\bar{6}m2$ No. 187	$P\bar{6}m2$ No. 187	$P6_3mc$ No. 186	$P6_3mc$ No. 186	$P6_3/m$ No. 176
a (pm)	286.8 (3)	285.3 (3)	573.56 (4)	573.953 (9)	489.24 (1)
c (pm)	281.0 (3)	278.9 (3)	562.81 (4)	561.76 (1)	1106.43 (4)
V (pm^3)	20.0 (2) × 10^6	19.7 (2) × 10^6	160.34 (2) × 10^6	160.263 (5) × 10^6	229.35 (1) × 10^6
Z	1	1	8	8	12
Range (deg)	10–90	10–90	10–90	10–117	10–117
R_p (%)	—	—	14.52	5.38	11.13
wR_p (%)	—	—	19.30	6.60	14.96

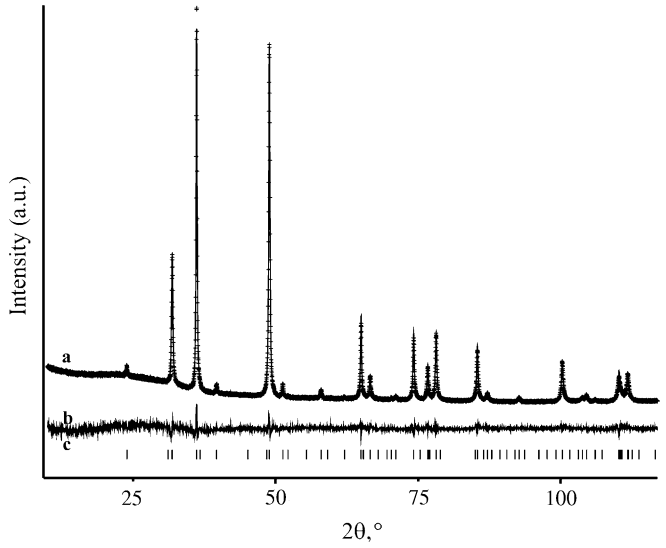

Fig. 4. Rietveld refinement results for the powder X-ray diffraction pattern of **F** prepared by ammonolysis of MoS_2: measured pattern (+) and the calculated curve for δ_3-MoN (solid line) (a); the difference between the two curves is plotted below (b) and the positions of reflections for the δ_3 phase are shown (c).

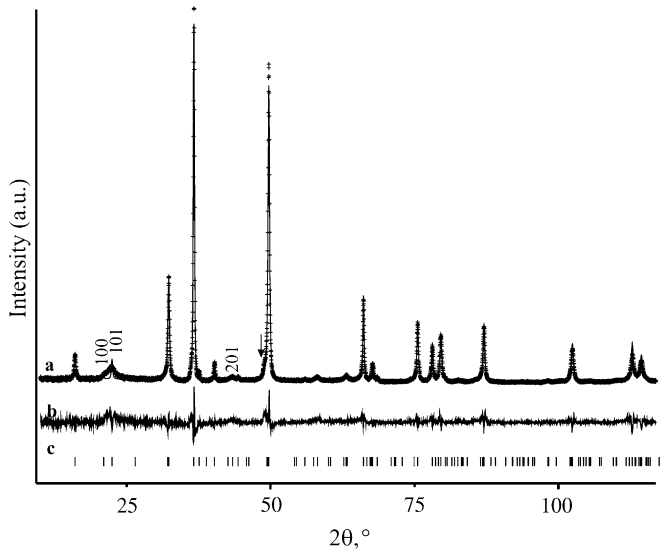

Fig. 5. Rietveld refinement results for the powder X-ray diffraction pattern of **D**: measured pattern (+) and the calculated curve (solid line) (a); the difference between the two curves is plotted below (b) and the positions of reflections for Mo_5N_6 are shown (c). An arrow marks an impurity reflection belonging to δ_3-MoN.

Table 3
Atomic positions in δ_3-MoN prepared from N_2 plasma and $MoCl_5$ at 730 °C (**B**)

Atom	Position	x	y	z	SOF
Mo1	2*a*	0	0	−0.010 (3)	1.0
Mo2	6*c*	0.4921 (2)	0.5079 (2)	−0.024 (3)	0.91 (2)
N1	2*b*	0.3333	0.6667	0.750 (6)	1.0
N2	6*c*	0.184 (3)	0.816 (3)	0.253 (4)	1.0

Table 4
Atomic positions in δ_3-MoN prepared by ammonolysis of MoS_2 (**F**)

Atom	Position	x	y	z	SOF
Mo1	2*a*	0	0	–0.009 (3)	1.0
Mo2	6*c*	0.4881 (1)	0.5119 (1)	–0.007 (2)	0.97(2)
N1	2*b*	0.3333	0.6667	0.757 (4)	1.0
N2	6*c*	0.165 (7)	0.835 (7)	0.263 (3)	1.0

Table 5
Atomic positions in Mo_5N_6 prepared by ammonolysis of MoS_2 (**D**)

Atom	Position	x	y	z	SOF
Mo1	2*a*	0	0	0.25	0.594 (9)
Mo2	2*b*	0	0	0	1.0
Mo3	2*c*	0.3333	0.6667	0.25	0.492 (9)
Mo4	2*d*	0.6667	0.3333	0.25	1.0
Mo5	4*f*	0.3333	0.6667	0.0029 (3)	1.0
N	12*i*	−0.013 (4)	0.356 (5)	0.124 (1)	1.0

and $P6_3/m$, the centrosymmetric space group $P6_3/m$ and the filled MoS_2-type structure previously suggested in [7] was chosen as a starting model for the structure of **D**. In this refinement, the isotropic temperature displacement factors had also to be fixed at $U_{iso} = 50\,pm^2$ for all atoms. Details of structure refinement and atomic position are displayed in Tables 2 and 5.

The details of the crystal structure investigations on δ-MoN and Mo_5N_6 may be obtained from Fachinformationszentrum Karlsruhe, 76344 Eggenstein-Leopoldshafen, Germany (fax: +49-7247-808-666; e-mail: crysdata@fiz-karlsruhe.de) on quoting the deposition nos. CSD-416438–416441.

2.6. Temperature-dependent Guinier measurements

The thermal stability of **C** and **D** was studied in the temperature range of 25–800 °C using a modified Simon–Guinier camera ($CuK\alpha_1$ radiation, $\lambda = 154.056\,pm$; quartz monochromator) [18]. For these investigations the samples were loaded in 0.3 mm quartz capillaries in the dry box and then sealed.

2.7. High-resolution transmission electron microscopy and selected area electron diffraction

A, **B**, **C**, and **E** were crushed in an agate mortar and suspended in *n*-butanol. A perforated carbon/copper net was covered with the suspension, leaving wedge-shaped crystallites in random orientation after drying. HRTEM and SAED investigations were performed on a Philips CM30ST (300 kV, LaB_6 cathode, $C_S = 1.15\,mm$) electron microscope. Computer simulations of the HRTEM images (multislice formalism) and SAED patterns (kinematical approximation) were carried out with the EMS programme

package [19] (spread of defocus: 70 Å, illumination semiangle: 1.2 mrad). All images were collected with a Multiscan CCD Camera (software Digital Micrograph 3.6.1 (Gatan)).

2.8. Magnetic susceptibility measurements

Measurements were carried out for **C**, **D**, and **F** using a Quantum Design MPMS SQUID magnetometer in the temperature range of 2–22 K and magnetic field of 6 mT. In a drybox 5–10 mg of compound was loaded into a previously dried (80 °C, 10^{-2} Torr) gelatine capsule. The capsule, transported in a Schlenk glass, was loaded into the magnetometer in a reverse argon flow. All three samples exhibited different superconducting behaviour as illustrated in Fig. 6.

3. Results and discussion

3.1. δ_1-MoN

The most plausible model for the crystal structure of the δ_1 phase can be introduced as a layer structure with a complex sequence of nitrogen layers, in which some pairs of adjacent layers of the same kind, e.g. AA, and the other alternating (AB). The metal atoms are then distributed in the trigonal prismatic or octahedral voids (γ) built by nitrogen atoms. Therefore, one can view this structure as a random stacking of the WC- and NiAs-type building blocks. According to this model, one should expect some amount of disorder in the real structure of **A** and **C** along the *c*-axis. In fact, the broadening of reflection lines and in particular the 0 0 *l* reflections in the PXRD patterns shown in Fig. 2 confirmed this assumption. The disordering along the *c*-axis was also corroborated by the difference of *c* parameter values observed for both samples (cf. Table 2). However, the results differed only slightly from each other. In order to test the proposed structure model for the δ_1-MoN, **A** and **C** were additionally investigated by HRTEM and SAED.

Samples **A** and **C** consisted of mostly disordered crystallites with a typical diameter of 50 nm. The SAED patterns recorded on such crystallites in [100] orientation showed very different scattering phenomena along the [001]* axis depending on the amount of disorder. In cases of a high density of stacking faults significant diffuse scattering streaks along the [001]* axis indicated the disordered nature of the real structure (cf. Fig. 7 left). However, in rare cases, we could observe the crystallites, whose SAED patterns could be assigned to those expected for δ_2-MoN (the diffuse scattering along the [001]* is weak) (cf. Fig. 7 right). Remarkably, the ordering occurred to a different extent in the same crystal as could be demonstrated in Fourier transforms of high-resolution images depicted in Fig. 8.

Interestingly, we also observed crystallites exhibiting a four-fold superstructure along [001] as a by-product in **A**. The lattice parameter ($c \sim 1120$ pm) agrees with the one observed for Mo_5N_6 phase. On the other hand, δ_3-MoN was not observed in **A** and **C**.

Temperature-dependent Guinier measurements carried out on **C** have shown that no transformation of δ_1-MoN to δ_3-MoN occurred below 800 °C at ambient pressure. On the other hand, the additional reflections in the resulting diffraction patterns of **C** indicated that δ_1-MoN begins to decompose to Mo_2N [20] at 770 °C. However, this decomposition of the δ_1 phase is a rather slow process: a complete conversion into Mo_2N occurred only after 120 h at the temperature of 800 °C, as can be shown by long-term annealing of **C** in a quartz capillary. No evidence of δ_3-MoN formation was observed in this experiment as well. Evidently, the transformation of the δ_1 phase into the δ_3

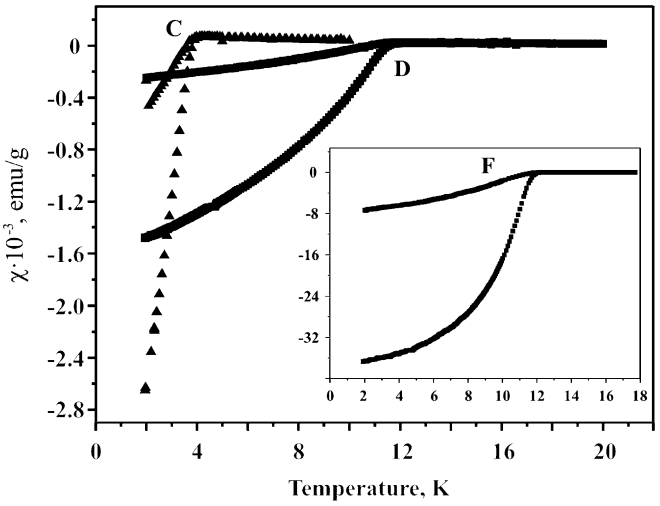

Fig. 6. Results of magnetic measurements on hexagonal molybdenum nitrides (ZFC and FC curves). The main figure illustrates temperature dependence of magnetic susceptibilities for **C** (▲) and **D** (■). The inset shows the data for **F**; it should be noted that the value of magnetic susceptibility is an order of magnitude larger than that observed for **C** and **D**.

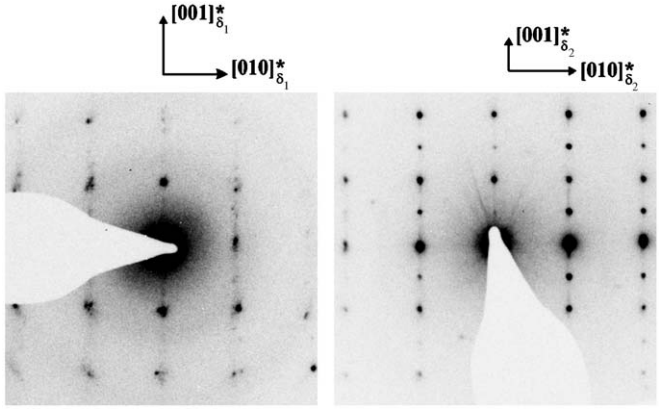

Fig. 7. SAED patterns in the zone axis [100] observed for **A** prepared from N_2 plasma and $MoCl_5$ by PECVD. Significant diffuse scattering along *c** in domains with a high density of stacking faults (left) and rare ordering of structure in otherwise disordered crystals of the δ_1-MoN (right). Similar results were found for **C** prepared by ammonolysis of $MoCl_5$.

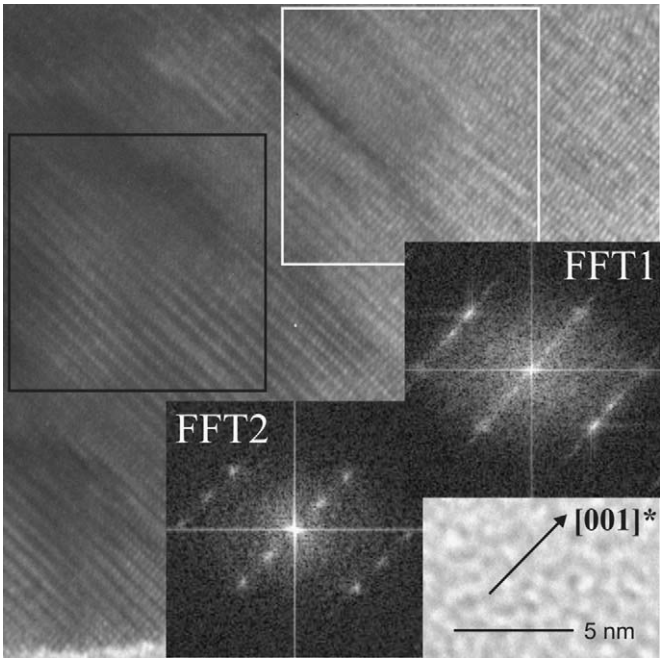

Fig. 8. HRTEM micrograph of a crystallite from **A**. FFT1 related to the δ_1-MoN and FFT2 correlating with δ_2-MoN are shown in the insets. The white and black squares mark FFT1 and FFT2 regions, respectively. Similar crystallites were observed in **C**.

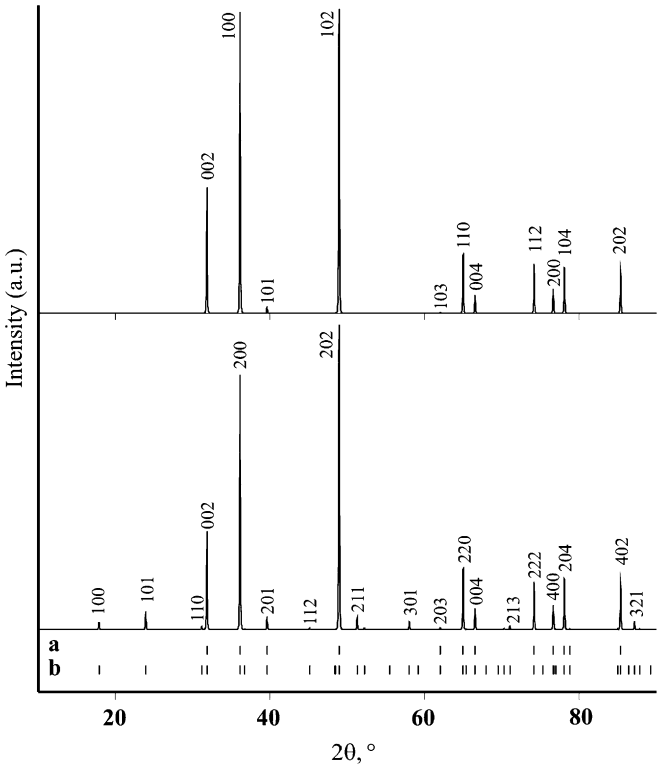

Fig. 9. The problem of distinguishing between δ_2-MoN (above) and δ_3-MoN (below) using powder X-ray diffraction. The PXRD diagram of the δ_3 phase contains weak superstructure reflections due to the formation of metal clusters. Positions of reflection lines are marked with bars for δ_2-MoN (a) and δ_3-MoN (b).

phase occurs only under high-temperature high-pressure conditions, as have been already reported earlier [6].

δ_1-MoN is superconducting with $T_c = 4\,K$ as shown by magnetic property measurements on **C** (cf. Fig. 6). This result agreed well with those reported previously [6,8]. However, for the sample of δ_1-MoN prepared at a higher temperature of 650 °C (cf. **C** prepared at 600 °C) we observe higher T_c: the sample became superconducting under 6 K.

3.2. δ_2-MoN

The PXRD patterns of **B** prepared from N_2 plasma and $MoCl_5$ by PECVD were consistent with that one expected for δ_3-MoN (cf. Fig. 3a). But, as illustrated in Fig. 9, due to the almost complete overlapping of the diffraction maxima for the δ_2 and δ_3 phases, one can be sure from the PXRD study only about the existence of δ_3-MoN in **B**. The line intensities are almost identical, which makes the separation of the two phase using Rietveld refinement almost impossible. However, the problem of phase analysis of these samples can be overcome by using electron diffraction on microcrystals. Therefore, the additional studies by HRTEM in a combination with SAED were carried out on **B**.

The sample consisted of thin plates, which were mostly perfectly ordered; no diffuse scattering was observed in recorded SAED patterns (cf. Fig. 10a). In rare case, the disordering of the structure could be observed corresponding to stacking faults along [001] (cf. Fig. 10b).

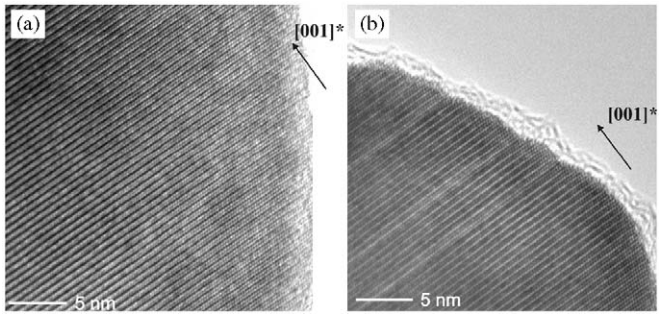

Fig. 10. HRTEM micrographs of crystallites in **B** prepared from N_2 plasma and $MoCl_5$ by PECVD. Perfect order (a) and stacking faults in the crystallites (b).

Simulations of electron diffraction patterns indicate the means as well as the limitations in distinguishing of δ_2- and δ_3-MoN. The existence of the δ_3 phase should be evident in most zone axes orientations of single crystals owing to additional reflections occurring with respect to the δ_2 phase (doubling of the *a*-axis due to the clustering of molybdenum atoms). Therefore, one should observe additional reflections along [010]* in the case of δ_3-MoN microcrystals. In fact, as shown by electron diffraction experiments, all crystals were found to contain two different ordering variants forming separate domains. These were

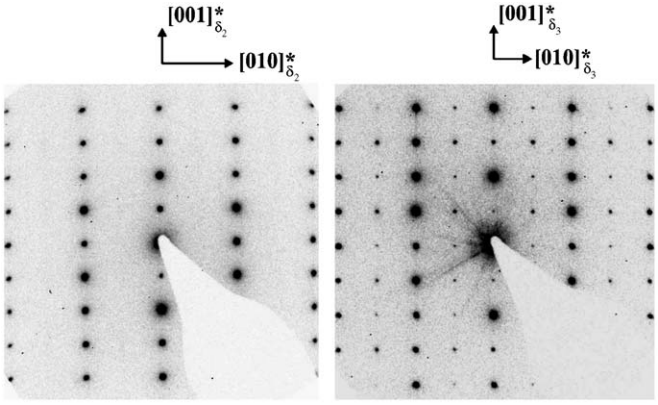

Fig. 11. SAED patterns in the zone axis [100] observed for **B** in different domains of the same microcrystal. Absence of superstructure reflection along $[010]^*$ is indicative of δ_2-MoN (left); these are present in the case of δ_3-MoN (right).

consistent with either δ_2-MoN or δ_3-MoN, as shown in Fig. 11 by SAED patterns. Thus, the anomalies observed by the Rietveld refinement of PXRD data, particularly, the high *R*-values (see Tables 2 and 3) could be rationalised by the double-phase character of **B**.

3.3. δ_3-MoN

The systematic absences in PXRD patterns of **B** and **F** were consistent with the space group $P6_3mc$ reported previously for δ_3-MoN [6–8]. Crystallographic data obtained by Rietveld refinement are summarised in Tables 2–4. Even though the unit cell parameters and positions of the atoms obtained for **B** were less accurate than those deduced from data for **F**, the difference in the *c* parameter values found for **B** and **F** was significant (cf. Table 2). However, this discrepancy could be rationalised, if one considers that according to SAED sample **B** contained δ_2-MoN with a longer *c* parameter value of 569 pm as a second phase. This could also explain somewhat longer intracluster Mo–Mo distances of 273.1(2) pm in **B** compared to those obtained for **F** (266.49(9) pm). The latter value is almost identical to those of 267 pm [7] and 267.1 pm [8] reported earlier.

δ_3-MoN becomes superconducting below 12 K as shown by magnetic measurements on **F** (cf. Fig. 6). The observed value of T_c agreed with those reported earlier [7,8].

3.4. Mo_5N_6

The measured PXRD pattern observed for **D** (Fig. 5a), the refined unit cell constants and atomic positions compared well with those reported earlier [7,21]. However, in order to reproduce all reflections in the diffraction pattern properly, we had to assume a different distribution of vacancies on Mo sites. These were suggested to be situated not in octahedral, but rather in trigonal prismatic voids (cf. Fig. 1b). Even when reflections 100, 101, and 201 marked in Fig. 5a were attributed to impurity phases, the model with vacancies in trigonal prismatic holes was still more accurate. Results of Rietveld refinement suggested that one-third of vacancies is distributed at random over trigonal prismatic sites (cf. Table 5). In this case, one could not explain the origin of the $\sqrt{3} \times \sqrt{3} \times 4$ superstructure, clearly observed from the PXRD data. Thus, sample **E** prepared by ammonolysis of MoS_2 and consisting of δ_3-MoN and Mo_5N_6 phases was investigated by HRTEM and SAED.

The composition of the sample was confirmed as mixture of the δ_3-MoN and Mo_5N_6 phases. Frequently, an intergrowth of both phases was observed (cf. Fig. 12). Both phases formed (001) stacks, which were intergrown coherently. Typical SAED patterns for δ_3-MoN are shown in Fig. 13. The superstructure reflections in SAED patterns shown in Fig. 14 correspond to those expected for Mo_5N_6, i.e. a four-fold superstructure along [001]* (left, zone axis [100]) and a $\sqrt{3} \times \sqrt{3}$ superstructure perpendicular to [001]* (right, zone axis [001]), in accordance with the superstructure reported in [7].

Results of HRTEM and SAED investigations suggested that even a small amount of δ_3-MoN in Mo_5N_6 samples leads to phase intergrowth also indicated by broadening of 1 0 0, 1 0 1, and 2 0 1 reflection lines in Fig. 5. In fact, a more detailed analysis of the PXRD pattern for **D**, originally believed to be a single-phase sample of Mo_5N_6, has shown

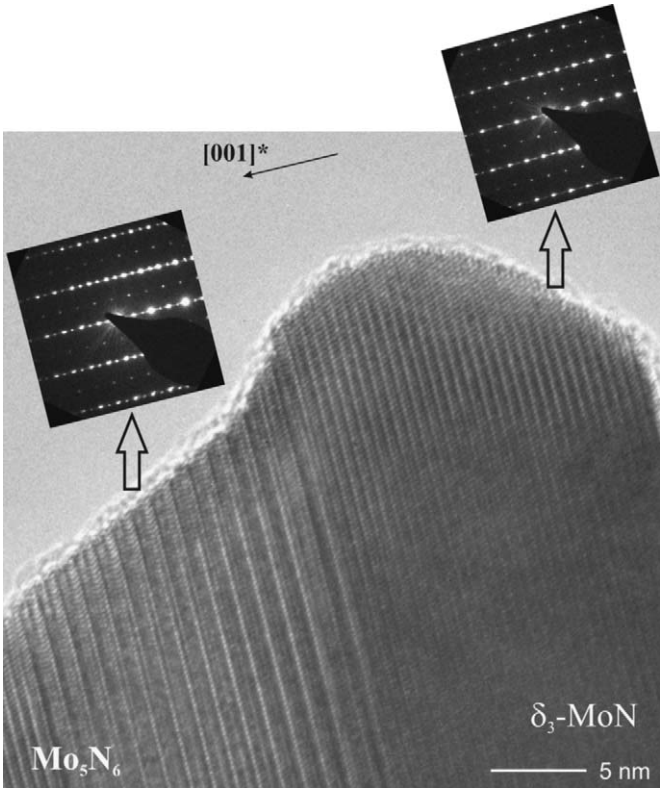

Fig. 12. HRTEM micrograph of one microcrystal from **E** prepared by ammonolysis of MoS_2 illustrating the intergrowth of δ_3-MoN and Mo_5N_6. SAED patterns related to δ_3-MoN and Mo_5N_6 are also shown.

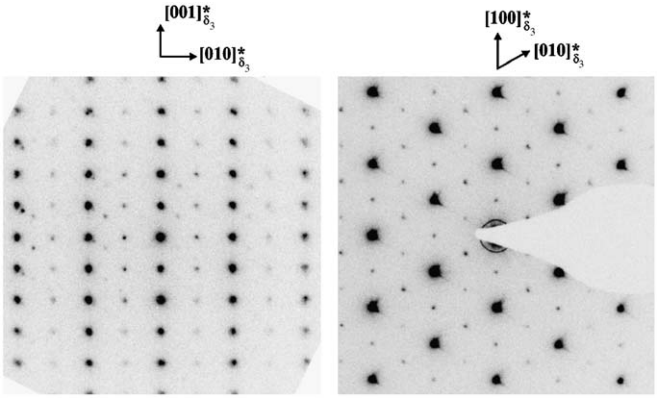

Fig. 13. SAED patterns of δ_3-MoN in the zone axes [100] (left) and [001] (right) observed in **E**.

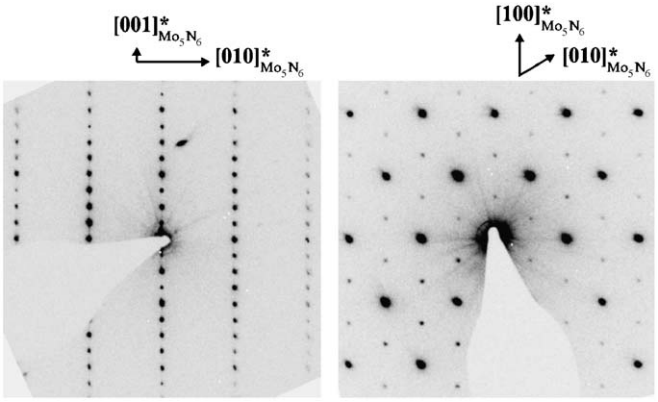

Fig. 14. SAED patterns of Mo_5N_6 in the zone axes [100] (left) and [001] (right) observed in **E**.

that the sample was contaminated by the δ_3 phase (indicated with an arrow in Fig. 5). This situation is reminiscent of sample **B** containing a mixture of δ_2- and δ_3-MoN: overlapping of the PXRD patterns might also explain some results of Rietveld refinements, e.g. the high *R*-values and no clear evidence for ordering of the vacancies in Mo_5N_6 (cf. Table 5).

In contrast to **B**, δ_2-MoN was never observed in **E** by HRTEM and SAED. As was noted in the previous section, the formation of δ_2-MoN was observed for **A**, **B**, and **C** all prepared by nitriding of $MoCl_5$ using PECVD and by the ammonolysis route, respectively. This suggested that δ_2-MoN can only be prepared from $MoCl_5$ in the temperature range between 610 and 730 °C, but not by ammonolysis of MoS_2, which takes place at temperatures above 750 °C.

Temperature-dependent Guinier measurements carried out on **D** showed the same result as in the case of **C** (δ_1-MoN): no phase transformation was observed up to 770 °C, followed by a decomposition to Mo_2N.

From the magnetic measurements on **D**, Mo_5N_6 is a superconductor with $T_c = 12$ K, which agrees with the previously reported value [7]. However, the diamagnetic response is relatively low suggesting that the superconductivity in Mo_5N_6 samples could be due to a contamination by the δ_3-MoN.

3.5. Conclusions

We conclude that it is possible to obtain three different forms of the hexagonal stoichiometric MoN—δ_1-, δ_2-, and δ_3-MoN—and one slightly overstoichiometric phase with composition Mo_5N_6 from N_2 and $MoCl_5$ using the PECVD method as well as by applying the conventional ammonolysis technique to $MoCl_5$ and MoS_2. The crystal structure of δ_1-MoN with stacking faults of N atom layers along the *c*-axis was introduced and then confirmed by PXRD, HRTEM, and SAED. Furthermore, there is no order–disorder transformation of δ_1-MoN into δ_3-MoN at ambient pressure. It was shown that δ_2-MoN with the NiAs-type structure could be prepared from $MoCl_5$ in the temperature range of 610–730 °C by nitriding under plasma conditions or by ammonolysis. However, δ_2-MoN could not be isolated as a single phase so far. Intergrowth of δ_3-MoN and Mo_5N_6 was observed and investigated by HRTEM and SAED. The results of Rietveld refinement suggest that the vacancies in Mo_5N_6 are distributed statistically in the trigonal prismatic holes built by nitrogen atoms.

Acknowledgments

This work was supported by the Sofja Kovalevskaja Research Award of the Alexander von Humboldt Foundation, the Federal Ministry of Education and Research, and Programme for Investment in the Future (ZIP) of the German Government. We thank Professor Arndt Simon for his support and critical comments on the manuscript, Viola Duppel and Claudia Kamella for EDXS and HRTEM measurements, and Willi Röthenbach for temperature-dependent Guinier measurements. We also thank Dr. Franck Tessier for helpful comments.

References

[1] W. Lengauer, J. Cryst. Growth 87 (1988) 295–298.
[2] A. Yu. Ganin, L. Kienle, G.V. Vajenine, Electrochem. Soc. Proc. 8 (2005) 449–456.
[3] A.Yu. Ganin, Dissertation, Stuttgart, 2005.
[4] G. Hägg, Z. Phys. Chem. B 7 (1930) 339–362.
[5] N. Schönberg, Acta Chem. Scand. 8 (1954) 204–207.
[6] A. Bezinge, K. Yvon, J. Muller, W. Lengauer, P. Ettmayer, Solid State Commun. 63 (1987) 141–145.
[7] R. Marchand, F. Tessier, F.J. DiSalvo, J. Mater. Chem. 9 (1999) 297–304.
[8] C.L. Bull, P.F. McMillan, E. Soignard, K. Leinenweber, J. Solid State Chem. 177 (2004) 1488–1492.
[9] F. Kadijk, F. Jellinek, J. Less-Common Met. 19 (1969) 421–430.
[10] H. Jehn, in: H. Katscher (Ed.), Gmelin Handbook of Inorganic Chemistry, eighth ed., Mo Supl. vol. B5, Springer, Berlin, 1990, pp. 46–52.
[11] W. Lengauer, in: R. Riedel (Ed.), Handbook of Ceramic Hard Materials, vol. 1, Wiley-VCH, Weinheim, 2000, p. 204.
[12] B.R. Sahu, L. Kleinman, Phys. Rev. B 70 (2004) 073103.

[13] N.V. Troitskaya, Z.G. Pinsker, Kristallografiya 8 (1963) 548–555.
[14] J. Beck, F. Wolf, Acta Cryst. B 53 (1997) 895–903.
[15] A. Yu. Ganin, L. Kienle, G.V. Vajenine, Eur. J. Inorg. Chem. (2004) 3233–3239.
[16] A.C. Larson, R.B. von Dreele, The General Analysis System (GSAS), Los Alamos National Laboratory Report LAUR 86 (2000); B.H. Toby, EXPGUI a graphical user interface for GSAS, J. Appl. Cryst. 34 (2001) 210–213.
[17] P. Stephens, J. Appl. Cryst. 32 (1999) 281–289.
[18] A. Simon, J. Appl. Cryst. 4 (1971) 138–145.
[19] P.A. Stadelmann, Ultramicroscopy 21 (1987) 131–145.
[20] D.A. Evans, K.H. Jack, Acta Cryst. 10 (1957) 833–834.
[21] F. Tessier, Dissertation, Rennes, 1996.